ROYAL SOCIETY
OF CHEMISTRY

Check for updates

Synergistic effect of GO/SrFe$_{12}$O$_{19}$ as magnetic hybrid nanocatalyst for regioselective ring-opening of epoxides with amines under eco-friendly conditions†

Mouhsine Laayati,[ab] Ayoub Abdelkader Mekkaoui, [ID][ab] Lahcen Fkhar,[b] Mustapha Ait Ali, [ID][b] Hafid Anane,[c] Lahoucine Bahsis, [ID][cd] Larbi El Firdoussi[b] and Soufiane El Houssame [ID] *[a]

Herein, a highly efficient magnetically separable hybrid GO/SrFe$_{12}$O$_{19}$ nanocomposite was synthesized *via* dispersing M-type strontium hexaferrite (SrFe$_{12}$O$_{19}$) on graphene oxide (GO) sheets. First, SrFe$_{12}$O$_{19}$ nanoparticles (NPs) and GO sheets were prepared *via* chemical coprecipitation and chemical oxidation of graphite powder, respectively. Chemically reduced GO (rGO) and rGO/SrFe$_{12}$O$_{19}$ were also prepared for comparison purposes. Thereafter, the prepared nanostructured materials were explored by XRD, FTIR, FESEM-EDX, BET, and Zetasizer analyses. All the characterizations confirm the nanoscale and the high stability structures of the prepared materials. The prepared hybrid magnetic nanocomposite GO/SrFe$_{12}$O$_{19}$ exhibited a high surface area value resulting in a high catalytic activity and selectivity for the epoxide ring-opening with amines in neat water. The use of hybrid GO/SrFe$_{12}$O$_{19}$ compared with pure SrFe$_{12}$O$_{19}$ and GO sheets is of great interest for using environmentally benign heterogeneous nanocatalysts, for the synthesis of β-amino alcohols, with excellent recyclability under eco-friendly conditions. Moreover, a mechanistic study was performed through density functional theory (DFT) calculations and Parr functions to explain the observed reactivity and selectivity of SrFe-GO catalyst in the epoxide ring-opening reactions.

1. Introduction

Nanotechnology is one of the most important research fields that covers various domains such as biology, medicine, agriculture, physics, chemistry, *etc.*[1–6] Over the last decade, this technology has been the target of fundamental and technological scientific research to develop new classes of nanostructured materials with unique properties and applications.[7–12] Among the interesting nanomaterials, hexagonal ferrites represent important classes of magnetic materials in diverse areas of applications such as plastic magnets, permanent magnets, recording media, microwave components, high-frequency devices, and catalysts or photocatalysts.[13–16] Since their discovery in the 1950s there has been an increasing degree of interest in the hexagonal ferrites,[17] and their synthesis and study deserve a particular interest for R&D researchers.[16,18–20]

However, magnetic nanoparticles (MNPs) have gained the attention of many scientists due to their excellent physical and chemical properties compared to traditional bulk materials, such as superparamagnetism, high surface area, high surface-to-volume ratio, simple separation under external magnetic fields, and high adsorption capacity.[21–26] Nowadays, it has been found that the dispersion of magnetic NPs on 2D materials such as graphene sheets is potentially turning into a new research topic due to their improved functionalities. Therefore, their use holds considerable promise for a wide range of applications in catalysis, biomedical fields, and for the removal of contaminants from wastewater.[27] Graphene, a single layer of carbon atoms packed in a two-dimensional honeycomb lattice, has a large surface area, open porous structure, flexibility, chemical stability, and very high electrical conductivity, which makes it a good candidate for the construction of graphene-based composite nanomaterials.[28–33]

[a]Laboratoire des Sciences des Matériaux, Mathématiques et Environnement, Université Sultan Moulay Slimane, Faculté Polydisciplinaire de Khouribga, BP 145, Khouribga 25000, Morocco. E-mail: hous_soufiane@hotmail.com; Fax: +212 523 490354; Tel: +212 523 490359

[b]Laboratoire de Chimie Moléculaire, Equipe de Chimie de Coordination et de Catalyse, Département de Chimie, Faculté des Sciences Semlalia, BP 2390, Marrakech 40001, Morocco

[c]Laboratoire de Chimie Analytique et Moléculaire, LCAM, Faculté Polydisciplinaire de Safi, Université Cadi Ayyad, Safi 46030, Morocco

[d]Laboratoire de Chimie de Coordination et d'Analytique (LCCA), Département de Chimie, Faculté des Sciences d'El Jadida, Université Chouaïb Doukkali, El Jadida, Morocco

† Electronic supplementary information (ESI) available. See https://doi.org/10.1039/d2ra00984f

In recent years, numerous hybrid composites have been synthesized based on strontium ferrite (SF) and reduced or non-reduced graphene oxide (rGO or GO) materials as heterogeneous catalytic systems. Recently, a nanocomposite based on polypyrrole/SrFe$_{12}$O$_{19}$/GO was used for the removal of tartrazine from wastewater.[34] However, Aziz et al. have reported the preparation of TiO$_2$-GO supported SrFe$_{12}$O$_{19}$ photocatalyst.[35] Additionally, J. Luo et al. have described the preparation of RGO/SF/PANI nanocomposites in a three-step synthesis as microwave absorber materials.[36] Besides, Zhao et al. produced rGO/SrFe$_{12}$O$_{19}$ nanocomposites by a two-step method for microwave absorption applications.[37]

The catalytic nucleophilic ring-opening of epoxides with amines represents one of the most important and straightforward methods for the preparation of β-amino alcohols as intermediates in the synthesis of a wide range of biologically active natural and synthetic products.[38–42] Recently, Y. He et al. have used epoxy ring-opening in a two-step synthesis of dimethyl carbonate by a coupling CO$_2$ cycloaddition and CH$_3$OH transesterification.[43,44] On the other hand, β-amino alcohols can be used as chiral ligands in various asymmetric syntheses.[45,46] Thus, enantioselective hydrogenation of arylalkyl ketones is possible using Ru(II)-fi-ferrocenyl amino alcohol catalyst.[47] It is noteworthy that these compounds have been widely employed for good enantioselectivity in Reformatsky reaction,[48] alkynylation of aromatic aldehydes,[49] or addition of divinylzinc.[50] Moreover, several Lewis or Brønsted acids were used as useful activators for better regioselectivity of epoxides aminolysis.[51–57] However, most of the existing methods involve high-cost processes, stoichiometric catalysts, corrosive reagents, and toxic metal ions and solvents. Therefore, it is desirable to develop new green procedures respecting the principles of green chemistry and circular economy.

Recently, we have reported M-type hexaferrite SrFe$_{12}$O$_{19}$ (SF) as an efficient heterogeneous bulk catalyst for amino alcohol synthesis.[58] To improve the catalytic activity of SrFe$_{12}$O$_{19}$, we have herein selected graphene oxide as dispersion of the catalytic active sites of SF due to its intriguing characteristics including high surface area, numerous oxygen-containing functional groups, high hydrophilicity, and good dispersion in water.

In this paper, we report the synthesis of SrFe$_{12}$O$_{19}$ nanoparticles using the coprecipitation method, and their combination with graphene oxide is carried out to study the synergistic effect of the hybrid nanocomposite (GO/SrFe$_{12}$O$_{19}$) on the catalytic activity of epoxide opening ring by amine to prepare β-aminoalcohols under eco-friendly conditions. Furthermore, GO, rGO, and rGO/SrFe$_{12}$O$_{19}$ nanomaterials were synthesized and evaluated for the catalytic epoxide ring-opening.

2. Experimental

2.1. Materials and chemicals

All reagents and solvents were purchased from commercial sources (Sigma Aldrich) and used as received without further purification: SrCl$_2$ (99.99%), FeCl$_3$·6H$_2$O (97%), NaOH (99.99%), graphite, sulfuric acid (98%), potassium permanganate (99.5%), and cetyltrimethylammonium bromide (CTAB).

2.2. Catalyst characterization

The X-ray powder diffraction (XRD) analysis was conducted on a D8 Discover Bruker (AXS) using CuKα radiation (λ_{Cu} = 1.5407 Å). FTIR analyses were recorded on ABB Bomem FTLA2000 in the range of 400–4000 cm^{-1} using KBr as a mulling agent. Raman spectra were conducted on Raman spectrometer (Confotec MR520), using a diode solid-state laser (618 nm) for irradiation. Microstructural characterizations were performed using a BRUKER (FEI, Quanta FEG 450) Scanning Electron Microscope (SEM) equipped with Energy Dispersive X-ray (EDX) detector. Zeta potential and size distribution were measured using a Malvern Panalytical Zetasizer, after dispersing 0.1 g of nanopowders in 3 mL of distilled water. The surface area of the SrFe$_{12}$O$_{19}$ and GO/SrFe$_{12}$O$_{19}$ was measured using a surface area analyzer (Micromeritics, ASAP 2010) at 77 K. Samples were degassed at 150 °C for 12 h under nitrogen flow to remove the moisture adsorbed on the solid surface. The mono-point BET method was used to evaluate the specific surface area (S_{BET}). Aliquots samples from the reaction mixture were monitored by Shimadzu gas chromatography (GC) with a flame ionization detector using nitrogen as a carrier gas. GC parameters for capillary columns BP (25 m × 0.25 mm, SGE): injector 250 °C; detector 250 °C; oven 70 °C for 5 min then 3 °C min^{-1} until 250 °C for 30 min; column pressure 20 kPa; column flow 6.3 mL min^{-1}; linear velocity 53.1 cm s^{-1}; total flow 138 mL min^{-1}. All obtained products were confirmed with an ISQ LT single quadrupole mass spectrometer operating in positive EI mode using a mass scan range of 50 to 400 m/z.

2.3. Materials synthesis

2.3.1. Synthesis of SrFe$_{19}$O$_{12}$. The SrFe$_{12}$O$_{19}$ MNPs were prepared as follows, stoichiometric amounts of metal chlorides were dissolved in 30 mL of deionized water separately to form homogeneous solutions which were mixed and stirred at 80 °C for 30 min. Afterward, the pH of the reaction mixture was adjusted to pH ≈ 11–12 by dropwise addition of 1.5 M of NaOH and kept on stirring for 1.5 h at 80 °C to guarantee the homogeneity of the mixture and to mix the reagents. The precipitated nanopowder was separated magnetically and washed several times with water to remove the execs of salts and dried at 80 °C overnight. The nanopowder was calcined at 1000 °C to obtain a pure strontium ferrite.

2.3.2. Synthesis of GO. The graphene oxide (GO) was prepared by treating graphite powder with potassium permanganate (KMnO$_4$, 99.5%) and concentrated sulfuric acid (H$_2$SO$_4$, 98%). After oxidation, the precipitate was collected by centrifugation and washed with deionized water and ethanol until neutral pH to remove metal ions and the excess unreacted acid. The obtained precipitate was separated and dried at 60 °C for 12 h.

2.3.3. Synthesis of hybrid GO/SrFe$_{19}$O$_{12}$. GO sheets were dispersed in deionized water and sonicated for 30 min, to stabilize the GO, cetyltrimethylammonium bromide (CTAB) was

added into GO solution in a continuous stirring to form a homogeneous dispersion (m(CTAB)/m(GO) = 1%). Then, M-type hexaferrite nanoparticles (SrFe$_{19}$O$_{12}$) were added to the dispersed solution in the weight ratio (10 GO/90 SF) and the mixture was stirred for 24 h. The resulting nanocomposite was separated magnetically and dried at 80 °C overnight under air.

2.3.4. Synthesis of rGO and rGO/SrFe$_{19}$O$_{12}$. The obtained GO sheets were dispersed in deionized water and sonicated for 30 min. Then, hydrazine hydrate (m(hydrazine hydrate)/m(GO) = 0.7) was added into the suspension and the mixture was stirred at 80 °C for 5 h. The suspension was washed using distilled water and ethanol. The resulting precipitate was separated, washed, and dried at 60 °C under vacuum for 12 h to obtain rGO. The same procedure was developed for the preparation of rGO/SrFe$_{12}$O$_{19}$ starting from the synthesized hybrid GO/SrFe$_{12}$O$_{19}$ nanocomposite.

2.4. General procedure for the catalytic epoxide ring-opening

The catalytic activity of the synthesized hybrid GO/SrFe$_{12}$O$_{19}$ nanocomposite was evaluated for the aminolysis of epoxides. The reaction was performed in a stoichiometric condition in presence of styrene oxide (0.66 mmol) and aniline (0.8 mmol) using GO/SrFe$_{12}$O$_{19}$ nanocomposite as catalyst (10 mg) and water as ecological solvent at 60 °C. The progress of the reaction was monitored using gas chromatography (GC). After the completion of the reaction, we observed the formation of foam due to the attack of amino groups at the acid functions of GO. Then, acetone was used to desorb the organic phase from the inorganic part. The catalysts were magnetically separated from the reaction mixture and were thoroughly washed with distilled water and acetone. The recovered catalysts were then dried and recycled for further use. The isolated products were analyzed using ^{1}H and ^{13}C NMR and GC-MS analysis.

2.5. Computational details

Quantum chemical calculations were performed by using GAUSSIAN 09W software[59] with the B3LYP method.[60,61] The LANL2DZ basis set was applied for the iron and strontium atoms,[62] and the 6-31G(d,p) for the other atoms. The global reactivity parameters such as electronic chemical potential (μ) and chemical hardness (η) are calculated using the frontier molecular orbital energies, HOMO (E_H) and LUMO (E_L), using the following expressions $\mu = (E_H + E_L)/2$ and $\eta = (E_L - E_H)$, respectively. At the same theoretical level, the global electrophilicity (ω) and nucleophilicity (N) indexes were calculated, and are given expressions: $\omega = \mu^2/2\eta$; $N = E_H - E_H$ (tetracyanoethylene (TCE)).[63,64] The Parr functions are calculated using the Mulliken atomic spin densities.[65] To get a closer understanding of the synergy effect between iron and strontium atoms for regioselective ring-opening of epoxides in the presence of amines, proposed models of the prepared catalyst were investigated using a DMol^3 module[66] of Material Studio 8.0. The optimization of metal clusters and adsorbing molecules were performed using the generalized gradient approximation (GGA) method[67] with the Perdew–Burke–Ernzerhof (PBE) function[68]

and the Double Numerical plus polarization (DNP) basis sets, which is comparable to Gaussian 6-31G(d,p).[69]

3. Results and discussion

3.1. Materials characterization

The phase purity and the stability of the synthesized materials were first investigated by XRD analyses (Fig. 1). As shown in Fig. 1a, the characteristic diffraction peaks of prepared GO corresponding to (001) and (101) planes were observed respectively at $2\theta = 10.66$ and $42.33°$, while the prepared rGO presents both characteristic diffraction patterns (002) and (111) respectively around $2\theta = 23.9$ and $42.9°$. In addition, the characteristic peak corresponding to (002) reflection plane of graphite was absent in both XRD spectra of GO and rGO. The XRD spectra of prepared SrFe$_{12}$O$_{19}$, hybrid GO/SrFe$_{12}$O$_{19}$, and rGO/SrFe$_{12}$O$_{19}$ present the same corresponding diffraction patterns of the M-type hexagonal SrFe$_{12}$O$_{19}$ phase and no other phases have been detected (Fig. 1b). Both prepared nanocomposites present crystalline SrFe$_{12}$O$_{19}$ in a hexagonal structure with a space group 194/$P63$ mmc, in good agreement with the standard JCPDF file (33-1340).[58,70] According to the Scherrer equation,[71] the crystallite size of the M-type hexagonal SrFe$_{12}$O$_{19}$ phase in the prepared SrFe$_{12}$O$_{19}$, hybrid GO/SrFe$_{12}$O$_{19}$, and rGO/SrFe$_{12}$O$_{19}$ were to be 25.098, 25.663, and 20.331 nm, respectively.

The FTIR spectra were recorded for GO, rGO, pure SrFe$_{12}$O$_{19}$, hybrid GO/SrFe$_{12}$O$_{19}$, and rGO/SrFe$_{12}$O$_{19}$ (Fig. 2). The results confirm the oxidation of graphite and clearly show the presence of oxygen-containing functional groups in graphite oxide such as O–H, C=O, and C–O. The spectrum of GO shows that the broad band appearing around 3395 cm^{-1} belonging to a strong stretching mode of OH group, the absorption band around 1723 cm^{-1} is attributed to C=O stretching mode, the absorption peak around 1620 cm^{-1} due to C=C stretching mode, and the large and less intense peaks around 1395, 1170, 1120, and 1057 cm^{-1} were assigned to the stretching modes of C–OH and C–O, respectively. Therefore, these groups are expected to form strong surface complexes with SrFe$_{12}$O$_{19}$ nanoparticles. However, the absence of the C=O absorption band and the increase of C–OH and C–O band intensities in the FTIR spectra of rGO and rGO/SrFe$_{12}$O$_{19}$ confirm the reduction of GO sheets. On the other hand, the spectrum of pure SrFe$_{12}$O$_{19}$ NPs shows the characteristic peaks of metal–oxygen bonds at 611, 555, and 449 cm^{-1}, respectively. These characteristic metal–oxygen peaks of SrFe$_{12}$O$_{19}$ arise from the vibrations of the hexaferrite structure.[72] The peak observed at 449 cm^{-1} may be attributed to Fe–O bending vibration in the octahedral site and the higher frequency band at 611 cm^{-1} could be associated with Fe–O stretching vibration of the tetrahedral site.[73] Moreover, the less intense peak that appeared at 555 cm^{-1} might be assigned to Sr–O bending vibration.[73,74] Thus, the spectrum of GO/SrFe$_{12}$O$_{19}$ (or rGO/SrFe$_{12}$O$_{19}$) exhibit the presence of all characteristic peaks of GO (or rGO) and SrFe$_{12}$O$_{19}$ in the hybrid, with a slight difference in the intensity of O–H, C=O, C–OH, and C–O (or O–H, C–OH, and C–O) peaks due to the interaction of hexaferrite NPs with the surface of GO (or rGO) sheets.
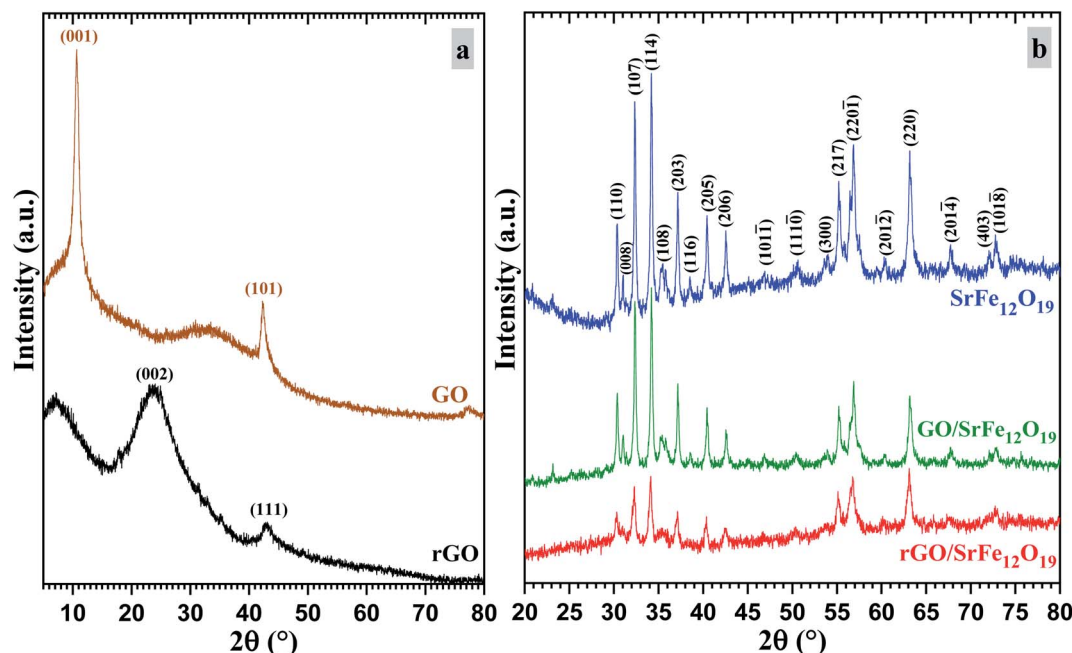
Fig. 1 XRD spectra of: (a) GO and rGO; (b) $SrFe_{12}O_{19}$, hybrid $GO/SrFe_{12}O_{19}$, and $rGO/SrFe_{12}O_{19}$.
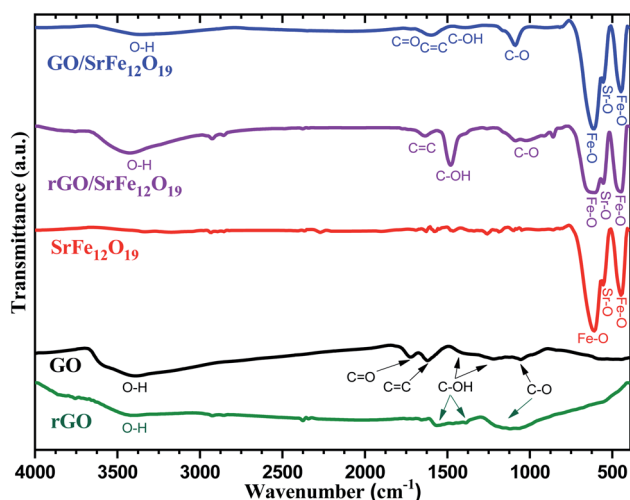
Fig. 2 FTIR spectra of rGo, GO, $SrFe_{12}O_{19}$, $rGo/SrFe_{12}O_{19}$, and hybrid $GO/SrFe_{12}O_{19}$.

The Raman spectra were measured for all prepared materials as shown in Fig. 3. The spectrum of $SrFe_{12}O_{19}$ is in good agreement with the data reported in the literature,[75,76] where the major peaks observed were around 689.48, 618.42, 535.24, 408.5 and 352.8 cm^{-1}. The spectra of GO, rGO, $GO/SrFe_{12}O_{19}$, and $rGO/SrFe_{12}O_{19}$ present two characteristic peaks of graphene materials corresponding to D-band at 1343.62 and G-band at 1593.14 cm^{-1}, due to the breathing mode of the k-point phonons with A_{1g} symmetry and first order scattering E_{2g} of the phonons from sp^2 carbon atoms, respectively. Moreover, the second order of zone boundary phonons or the 2D band which is related to the nature of the graphene layer stacking was

observed around 2702 cm^{-1} for GO. However, the I_D/I_G ratio increased from 0.93 in GO to 1.12 in rGO, which is due to the elimination of oxygen functionalities and the decrease in the average sp^2 domain size in rGO.[77] The I_D/I_G values of $GO/SrFe_{12}O_{19}$ about 1.01 and $rGO/SrFe_{12}O_{19}$ about 1.05 are lower than rGO value, owing to the lower degree of defects in the nanocomposites.

The morphology and the shape of the prepared pure $SrFe_{12}O_{19}$, GO, and rGO sheets were identified by FESEM analyses (Fig. 4). Moreover, the dispersion and the distribution of the deposited $SrFe_{12}O_{19}$ nanoparticles on GO or rGO sheets were also checked (Fig. 4). The analysis of pure $SrFe_{12}O_{19}$ FESEM images shows a nanostructured grain of the M-type
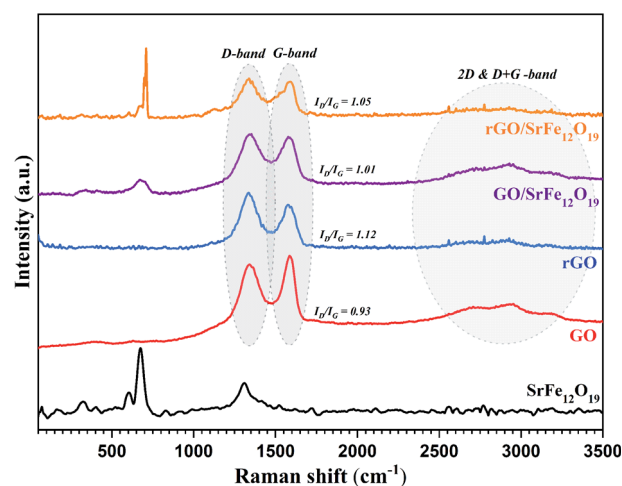

Fig. 3 Raman spectra of $SrFe_{12}O_{19}$, GO, rGO, $GO/SrFe_{12}O_{19}$, and $rGO/SrFe_{12}O_{19}$.
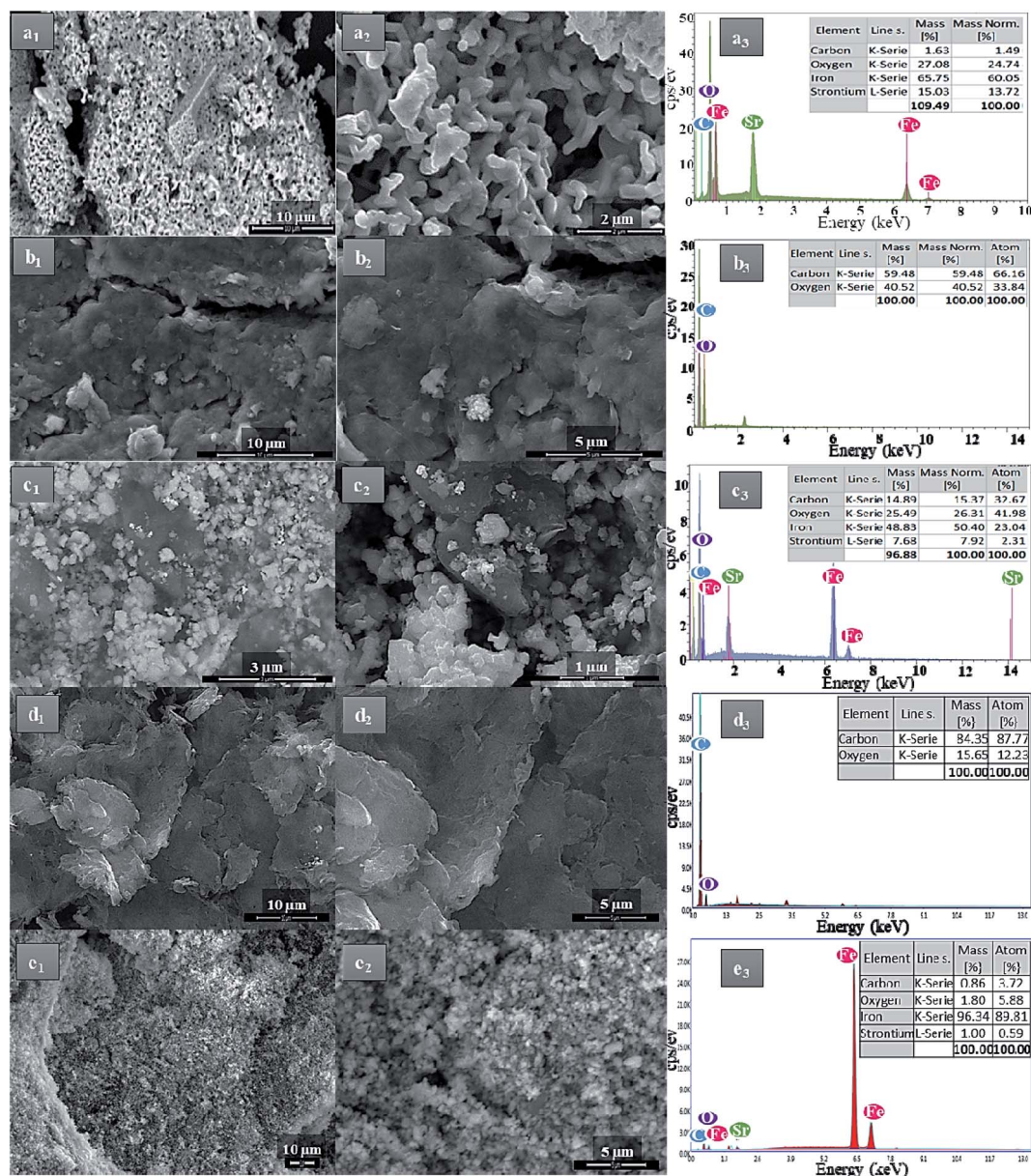
Fig. 4 FESEM-EDX analyses of (a) $SrFe_{12}O_{19}$, (b) GO, (c) hybrid $GO/SrFe_{12}O_{19}$, (d) rGO, and (e) $rGO/SrFe_{12}O_{19}$.

hexaferrite in a regular distribution of size and morphology (Fig. 4a1 and a2). The FESEM images of GO and rGO show the preparation of microstructured sheets in a good typical morphology (Fig. 4b1, b2, d1 and d2). While the hybrid $GO/SrFe_{12}O_{19}$ and $rGO/SrFe_{12}O_{19}$ images show hexaferrite nanoparticles in good dispersion and distribution at the nanoscale range on the surface of GO and rGO sheets (Fig. 4c1, c2, e1 and e2). However, The EDX analyses of all prepared materials show good homogeneity and purity in the chemical composition (Fig. 4a3–e3).

3.2. Catalytic epoxide ring-opening reaction

First, $SrFe_{12}O_{19}$ and the hybrid $GO/SrFe_{12}O_{19}$ nanomaterials are evaluated in the catalytic ring-opening of epoxide with various amines. In order to optimize the reaction conditions, we examined first the reaction in the presence of styrene oxide and aniline, chosen as model substrates (Scheme 1).

The catalytic performance of the prepared nanomaterials, $SrFe_{12}O_{19}$ and hybrid $GO/SrFe_{12}O_{19}$, was first evaluated in free-solvent conditions (Table 1).[58] As shown in Table 1, the epoxide was converted to the resulting ring-opening products in good yields (entries 1 and 2). However, the presence of $GO/SrFe_{12}O_{19}$ improved the selectivity by reducing the reaction time and showing a complete conversion. Consequently, the hybrid $GO/SrFe_{12}O_{19}$ exhibited an excellent catalytic performance than pure $SrFe_{12}O_{19}$, owing to the outstanding improvement in the catalytic activity of SF NPs while combined with GO sheets. The improvement of the catalytic activity can be explained by the GO environment that prevents unwished aggregation of SF NPs,[78]
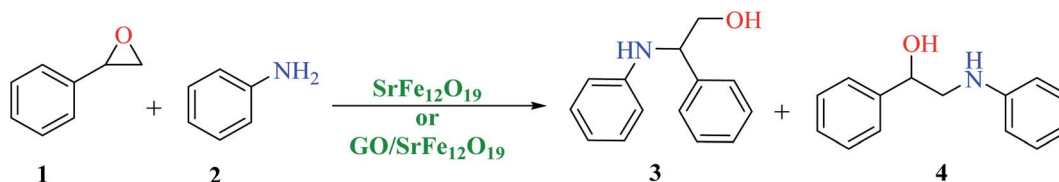
Scheme 1 Catalytic epoxide ring-opening of styrene oxide in presence of aniline catalyzed by $SrFe_{12}O_{19}$ or $GO/SrFe_{12}O_{19}$.

Table 1 $SrFe_{12}O_{19}$ and $GO/SrFe_{12}O_{19}$ catalytic activity in epoxide ring-opening[a]

Entry	Catalyst	Wt (g)	Solvent	Time (h)	Conversion[b] (%)	Selectivity 3[c] (%)	Selectivity 4[c] (%)
1	$SrFe_{12}O_{19}$	0.01	Neat	17	95	74	26
2	$GO/SrFe_{12}O_{19}$	0.01	Neat	5	100	92	8
3	$GO/SrFe_{12}O_{19}$	0.01	Water	2	100	92	8
4	$SrFe_{12}O_{19}$	0.01	Water	2	39	90	10

[a] Reaction conditions: styrene oxide (0.8 mmol), aniline (1 mmol), and 60 °C. [b] Conversion was determined by GC. [c] Selectivity was determined by GC.

and increase the active surface area of the hybrid nanomaterial compared to pure $SrFe_{12}O_{19}$, providing a good dispersion and distribution of SF. The use of water as a solvent in the presence of hybrid $GO/SrFe_{12}O_{19}$ improves the ring-opening reaction and 100% conversion was obtained after only 2 h of reaction time (entry 3). We can assume that an interaction of GO sheets with water molecules through hydrogen bonding[79] is probably involved in the reaction, proven by a lower conversion given with pure SF (entry 4). Moreover, water as a solvent promotes hydrogen bonding with the oxygen of epoxides which enhances the electrophilicity of the carbon in the alpha position.[80]

To shed more light on the effect of water as a solvent on the catalytic reaction and the stability of nanocomposites, zetasizer measurements of pure $SrFe_{12}O_{19}$ and hybrid $GO/SrFe_{12}O_{19}$ nanomaterials after their dispersion in water have been carried out (Table 2). The zeta potential (ZP) is applied for the determination of the surface charge of nanoparticles in colloidal solution and the ZP value can be related to the short- and long-term stability of nanoparticles in the studied colloidal solution.[81] For this purpose, we have used ZP to evaluate the stability of the developed nanomaterials in water as a green and ecological solvent. The pure $SrFe_{12}O_{19}$ and hybrid $GO/SrFe_{12}O_{19}$ nanomaterials gave a ZP of −24.8 and −18 mV, respectively. It has been reported that nanoparticles having −25 > ZP > +25 mV usually present a high degree of stability,[82] which means that pure $SrFe_{12}O_{19}$ is close to the threshold of agglomeration in

water. Recently, we have reported the non-adaptability of water as a solvent for the ring-opening of epoxide while using $SrFe_{12}O_{19}$ as a catalyst.[58] In contrast, the ZP value of hybrid $GO/SrFe_{12}O_{19}$ indicates its high stability in water, confirming the good choice of GO sheets for the dispersion of $SrFe_{12}O_{19}$ nanoparticles, which will be of great advantage for a greener catalytic application. On the other hand, the size peaks and z-average confirm the nanoscale size of hexaferrite nanoparticles and the microscale of GO sheets (confirmed by the increase in size and z-average of $GO/SrFe_{12}O_{19}$ sample). Consequently, the excellent catalytic performance of hybrid $GO/SrFe_{12}O_{19}$ in presence of water as an ecological solvent may be explained by the good dispersion of the hybrid nanomaterial in water compared to pure SF (ZP values). Moreover, hybrid $GO/SrFe_{12}O_{19}$ has a high specific surface area of ($134 \ m^2 \ g^{-1}$) compared to pure SF NPs ($25 \ m^2 \ g^{-1}$) (Table 2), which provide well dispersed and distributed active sites for adsorption of reactants.

We have also checked the effect of temperature on reaction rate (Fig. 5). The best optimum was to be 60 °C. The Fig. 5 shows also that the decreasing of the temperature resulted in lower conversion.

Systematic investigations on catalyst amounts were undertaken (Fig. 6). The best catalytic performance was obtained with 10 mg of catalyst. In contrast, in the absence of catalyst, only 16% of conversion and selectivity was obtained. The use of an

Table 2 Zetasizer measurements of dispersed nanomaterials in water and BET surface area

Nanocatalyst	Zeta potential (mV)	Size peaks		Z-Average (d nm)	BET surface area ($m^2 \ g^{-1}$)
		Size (d nm)	Intensity (%)		
$SrFe_{12}O_{19}$	−24.8 (±5.5)	0.651 (±0.045)	74.1	11.69	25
		2.999 (±0.358)	25.9		
$GO/SrFe_{12}O_{19}$	−18.0 (±3.62)	223.6 (±37.93)	82.6	166.4	134
		1.429 (±0.097)	17.4		
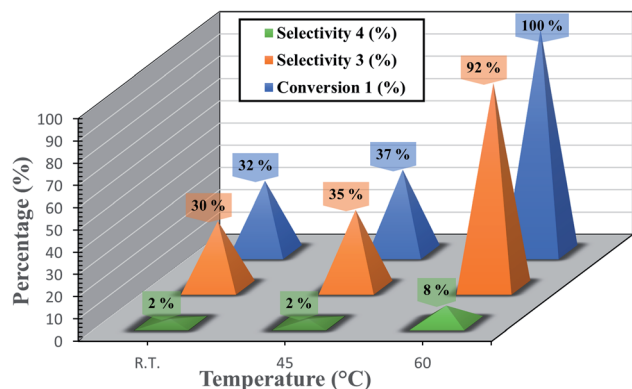
Fig. 5 Effect of temperature.

Fig. 6 Effect of catalyst amount.

While in presence of $SrFe_{12}O_{19}$ and rGO, only 39% and 16% of conversion was observed respectively (entries 2 and 4). These results clearly demonstrate that SF NPs and acid sites of GO sheets could be both considered as active sites (entry 3). However, rGO/$SrFe_{12}O_{19}$ nanocomposite gives the same result as the pure hexaferrite NPs. Indeed, Vithalani et al. have reported that the outcome of the catalytic activity presents a mediocre performance in presence of chloro-functionalized GO compared to GO due to lesser acidic sites on the surface of the catalyst.[83] Consequently, the combination of GO sheets with hexaferrite NPs effectively enhanced the catalytic activity and reusability of the developed catalyst, owing to the synergistic effect of GO and $SrFe_{12}O_{19}$ in a single magnetically separable nanostructured catalyst (hybrid GO/$SrFe_{12}O_{19}$ nanocomposite).

The scope and limitations of the developed hybrid catalytic system GO/$SrFe_{12}O_{19}$ were investigated in the catalytic epoxide ring-opening of styrene oxide in presence of various aromatic and aliphatic amines under the optimized conditions (Scheme 2). The results obtained are collected in Table 4.

As shown in Table 4, with all studied aromatic and aliphatic amines, styrene oxide was converted to the corresponding β-aminoalcohol products in moderate to excellent selectivity. The reaction was faster (2 h) compared to our previous work (17 h).[58] The regioselectivity of the catalytic reaction is influenced by the electronic and steric factors associated with both studied substrates epoxide and amines.[84] In presence of aromatic amines, the opening reaction is mainly oriented towards amino alcohols **5** through the nucleophilic attack at the benzylic carbon atom of the epoxide ring (entries 1–4). In addition, aniline with electron-withdrawing group substituents at *ortho* position reduced the conversion with good regioselectivity of 96% compared to unsubstituted one (entries 1–4). On the other hand, aliphatic amines oriented the regioselectivity towards amino alcohols **6** through the nucleophilic attack at the β position of the
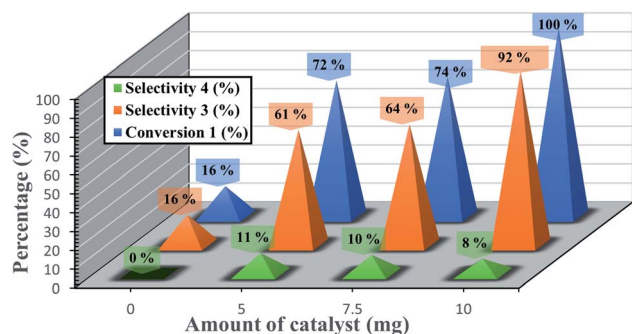
amount of 5 or 7.5 mg of catalyst resulted in a decrease of the conversion of epoxide to 72 and 74% respectively.

A Comparison of the catalytic activity of the prepared nanomaterials was performed (Table 3). When the reaction is carried out with GO, a good conversion was obtained (entry 1).

Table 3 Comparison of catalytic activity of prepared nanomaterials in catalytic epoxide ring-opening[a]

Entry	Catalyst	Conversion[b] (%)	Selectivity **3**[c] (%)	Selectivity **4**[c] (%)
1	GO	78	94	6
2	$SrFe_{12}O_{19}$	39	90	10
3	GO/$SrFe_{12}O_{19}$	100	92	8
4	rGO	16	100	0
5	—	16	100	0
6	rGO/$SrFe_{12}O_{19}$	37	100	0

[a] Reaction conditions: styrene oxide (0.8 mmol), aniline (1 mmol), catalyst (10 mg), solvent (water), and 60 °C for 2 h. [b] Conversion was determined by GC. [c] Selectivity was determined by GC.
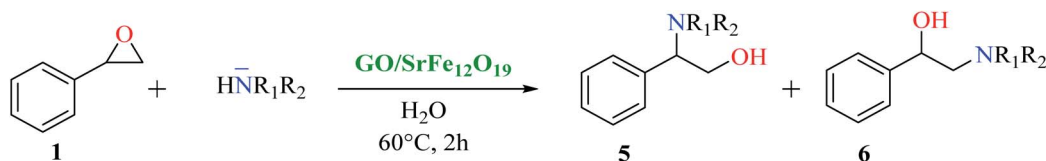

Scheme 2 Catalytic epoxide ring-opening of styrene oxide with various amines in presence of GO/$SrFe_{12}O_{19}$.

Table 4 Catalytic ring-opening of styrene oxide with various amines[a]

Entry	Amine	Major product	Conversion[b] (%)	Selectivity 5[c] (%)	Selectivity 6[c] (%)	Isolated yield[d] (%)
1			100	92	8	97
2			80	96	4	76
3			92	96	4	88
4			77	96	4	70
5			100	00	100	99
6			95	37	63	91
7			100	26	74	98

[a] Reaction conditions: styrene oxide (0.83 mmol), amine (1 mmol), GO/SrFe$_{12}$O$_{19}$ (10 mg), solvent (Water), and 60 °C for 2 h. [b] Conversion was determined by GC-MS. [c] Selectivity was determined by GC-MS. [d] Isolated yield of **5** and **6**.

benzylic carbon atom of the epoxide ring due to the steric effect (entries 5–7). Moreover, morpholine substrate totally oriented the regioselectivity with a complete conversion towards the corresponding amino alcohol **6** (entry 5).

The ratio of both regioisomeric products was determined by GC-MS (MS spectra in ESI†). The regioisomer of α-product (**3**) exhibited a molecular ion at m/z of $M^+ = 31$ due to the CH$_2$OH, and the regioisomer β-product (**4**) exhibited a molecular ion at m/z of $M^+ = 106$ arising from the loss of PhCHO.[85]

To examine the extension of the reaction, we have investigated the catalytic reaction of cyclohexene oxide with various aromatic and aliphatic amines under optimized conditions (Scheme 3). With all studied amines, cyclohexene oxide was converted to the corresponding β-amino alcohols in excellent yields (Table 5). According to ^{1}H NMR analyses (data and

spectra in ESI†), exclusive trans amino alcohol derivatives were obtained in the cleavage of the epoxide ring of cyclohexene oxide, which is in good agreement with the literature.[84,86] The trans stereoselectivity is confirmed by the high coupling constants (^3J) between the relevant HCOH and HCNR$_1$R$_2$ peaks present in the region of 2.44–4.13 ppm, in contrast to the lower ^3J between HOCH–CH$_{(cis)}$ and R$_1$R$_2$NCH–CH$_{(cis)}$.[87]

Ferrites as magnetic materials by nature point out their presence in heterogeneous catalysis as a highly recyclable catalyst. The recyclability performance of the developed catalytic system GO/SrFe$_{12}$O$_{19}$ as hybrid MNPs, was performed with styrene oxide and aniline under the optimized reaction conditions (Fig. 7). The catalyst was separated from the reaction mixture by applying an external magnetic field and reused for ten runs without significant loss in catalytic activity. After each run, the recycled catalyst was washed with water (3 × 5 mL) and acetone (3 × 5 mL) and dried at 100 °C for 3 h.

After the last run, the identity of the recovered hybrid nanocatalyst GO/SrFe$_{12}$O$_{19}$ was checked by zetasizer measurements, SEM-EDX, and XRD analyses (Table 6 and Fig. 8). The ZP of the recycled catalyst after 10 runs is close to the threshold of stability in water with an increase of z-average size, which could explain the slight loss of selectivity from 92% to 80% of amino alcohol **3** (Fig. 7). However, SEM images showed good stability
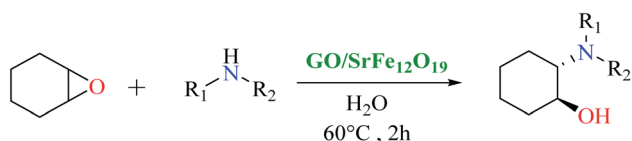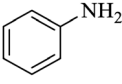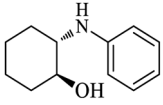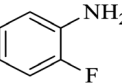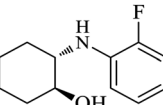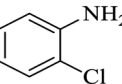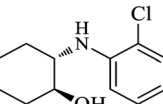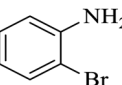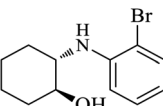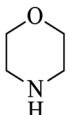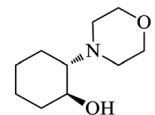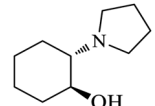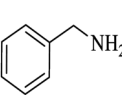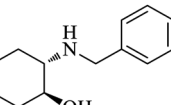
Scheme 3 Catalytic epoxide ring-opening of cyclohexene oxide in presence of various amines.

© 2022 The Author(s). Published by the Royal Society of Chemistry

Table 5 Catalytic ring-opening of cyclohexene oxide with various amines[a]

Entry	Amine	Product	Conversion[b] (%)	Selectivity[c] (%)	Isolated yield (%)
1	(aniline, NH_2)	(product, H–N–phenyl, OH)	100	100	97
2	(2-fluoroaniline, NH_2, F)	(product, H–N–2-fluorophenyl, OH)	100	100	95
3	(2-chloroaniline, NH_2, Cl)	(product, H–N–2-chlorophenyl, OH)	100	100	95
4	(2-bromoaniline, NH_2, Br)	(product, H–N–2-bromophenyl, OH)	100	100	95
5	(morpholine, O, N, H)	(product, morpholino, OH)	100	100	99
6	(pyrrolidine, NH)	(product, pyrrolidino, OH)	97	100	94
7	(benzylamine, NH_2)	(product, H–N–benzyl, OH)	100	100	95

[a] Reaction conditions: cyclohexene oxide (1.02 mmol), amine (1.1 mmol), GO/SrFe$_{12}$O$_{19}$ (10 mg), solvent (water), and 60 °C for 2 h. [b] Conversion was determined by GC-MS. [c] Selectivity was determined by GC-MS.

in the distribution and dispersion of SrFe$_{12}$O$_{19}$ NPs on GO sheets (Fig. 8a and b). In addition, EDX analysis confirms the stability in the elemental composition of hybrid GO/SrFe$_{12}$O$_{19}$ (Fig. 8c). Moreover, XRD patterns of the recovered nanocatalyst after ten runs show good crystalline stability compared to the fresh nanocatalysts GO/SrFe$_{12}$O$_{19}$ (Fig. 8d).
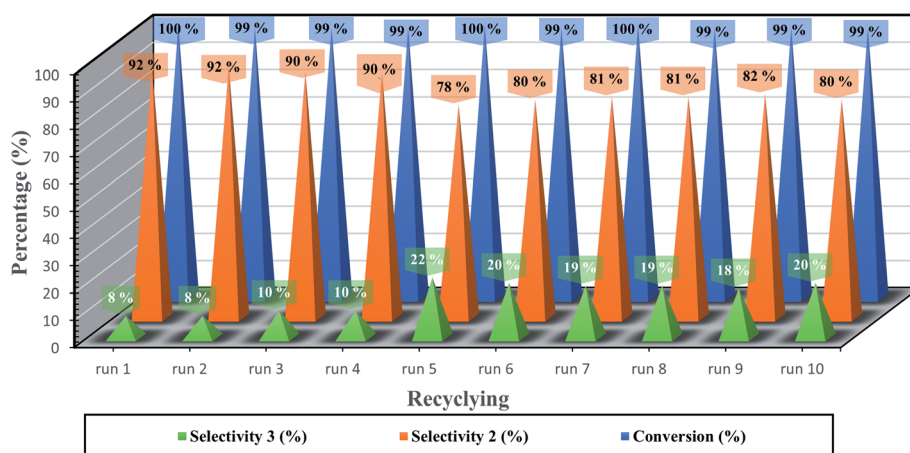
Fig. 7 Recyclability of hybrid GO/SrFe$_{12}$O$_{19}$ nanocomposites for the ring-opening of epoxide.

Table 6 Zetasizer measurements and crystallite size of $SrFe_{12}O_{19}$ in the hybrid before and after 10 runs

$GO/SrFe_{12}O_{19}$	Zeta potential (mV)	Z-Average (d nm)	SF crystallite size (nm)
Fresh	−18.0 (±3.62)	166.4	25.66
Recycled	−24.6 (±3.35)	272	26.01

3.3. Comparison of catalytic performance with other catalytic systems

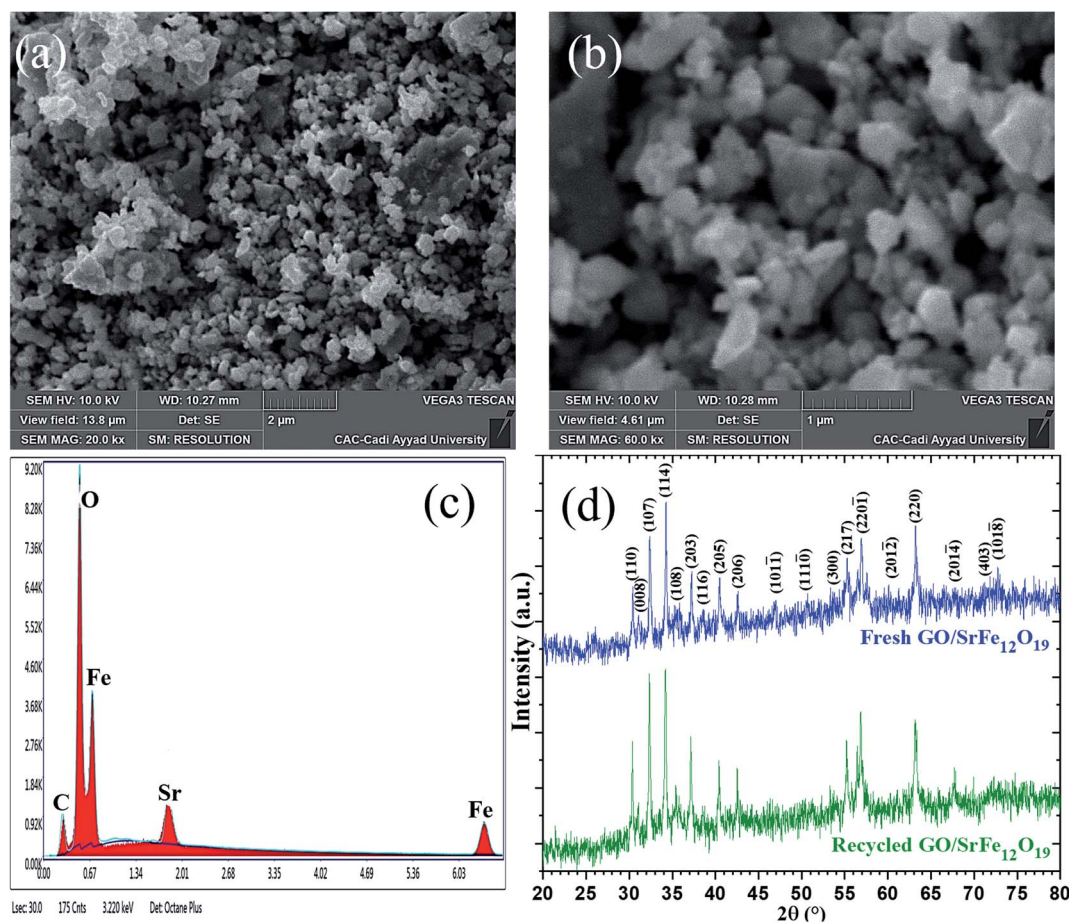A comparison of the catalytic performance of the hybrid GO/$SrFe_{12}O_{19}$ nanocatalysts with recent literature reports on styrene oxide ring-opening catalyzed by various catalytic systems is given in Table 7.

3.4. Mechanistic study

The catalytic activity of the hybrid GO/$SrFe_{12}O_{19}$ nanocomposite is mainly due to the metal ions present in the octahedral and tetrahedral sites,[92] and the oxygen functionalities dispersed on GO sheets could be responsible for their catalytic activity.[93] When the epoxide molecules are adsorbed on the surface of deposited hexaferrite, the acidic sites of hexaferrite and graphene oxide are activated (Scheme 4). The formation of the regioisomeric product arising from the nucleophilic attack on

Fig. 8 SEM images (a and b), EDX (c), and XRD (d) of recycled hybrid GO/$SrFe_{12}O_{19}$ after 10 runs.

Table 7 Comparison of catalytic performance of developed GO/$SrFe_{12}O_{19}$ nanocatalysts with other catalytic systems reported in literature

Catalyst	Reaction conditions	Conversion **1** (%)	Selectivity **3** (%)	Reusability (conversion : run)	Ref.
$Ni(S_2COCH_3)_2$	1 eq. amine, CH_2Cl_2, RT, 24 h	98	83	—	88
MS-AI	2 eq. amine, toluene, 50 °C, 4 h	92	98.5	—	89
Zr-MOR zeolite	1 eq. amine, free-solvent, 40 °C, 4 h	90.2	93.1	90.2 : 5	90
PTS-Im-3@GO	10 eq. amine, free-solvent, 50 °C, 4 h	100	100	94 : 5	91
$SrFe_{12}O_{19}$	1.1 eq. amine, free-solvent, 60 °C, 17 h	95	74	71 : 5	58
GO/$SrFe_{12}O_{19}$	1.1 eq. amine, water, 60 °C, 2 h	100	92	100 : 10	This work
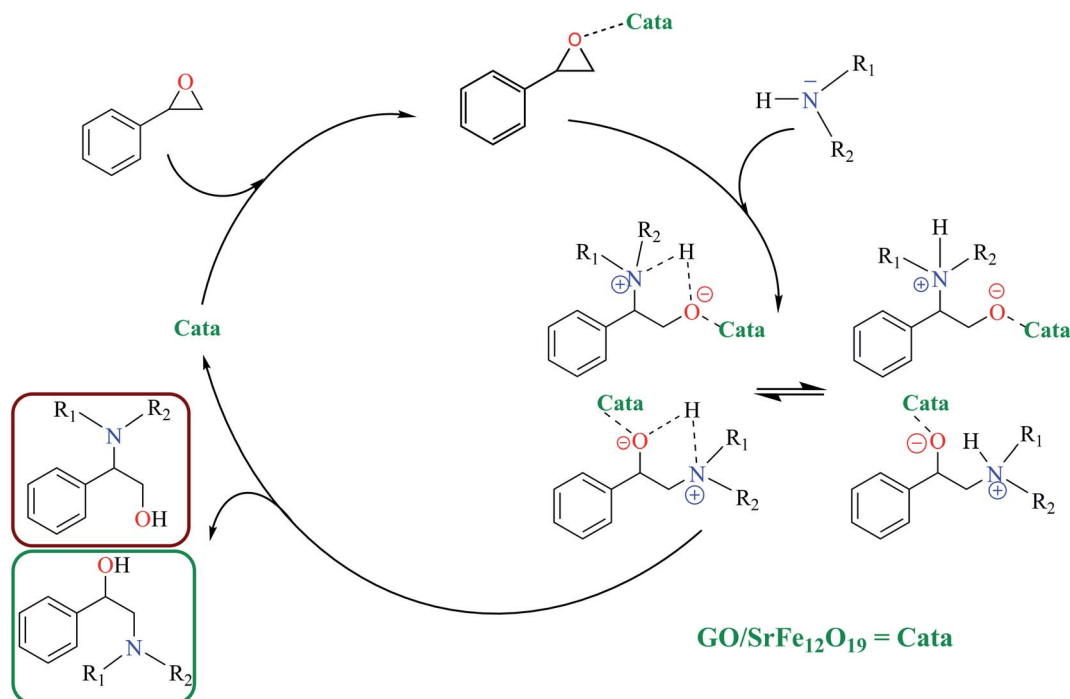
Scheme 4 Proposed mechanism for the catalytic ring-opening of styrene oxide.

the electron-deficient carbon atom of the epoxide is produced. In fact, the phenyl group in styrene oxide assists in the stabilization of carbocationic character at the benzylic carbon.

The epoxide ring-opening reaction in the presence of the prepared catalyst gives two possible products regarding the nature of the used amine compounds, as shown in the proposed mechanism (Scheme 4). Recently, we have used density functional theory (DFT) calculations to understand observed regio- and chemoselectivity during a studied catalytic reaction as well as the corresponding mechanistic pathway.[94] To get a closer understanding of the experimental results, DFT calculations were performed using models for the prepared nanocatalyst (Scheme 5). Initially, the optimized structures of single iron and strontium atoms with 2POX, and 2POX–AcOOH complexes were performed and illustrated in Fig. 9. The coordination energy for the formation of 2POX–metal complexes is positive, which indicates that the coordination reaction between metals and 2-phenyloxirane is endothermic (Fig. 9). However, the coordination energy of the 2POX–Fe complex is lower compared to the 2POX–Sr complex, leading to the conclusion that the coordination between 2POX and Fe metal is a more stable structure of

the 2POX–SrFe complex. For 2POX–AcOOH, the free energy for the formation of this complex is negative due to the hydrogen bond between AcOOH and oxygen of the epoxide ring.

The global reactivity indexes were used as a powerful tool for the theoretical understanding which can enable to explain the regio- and chemoselectivity reactions based on the measurement of the global electron density transfer (GEDT) value.[95,96] In this regard, the global properties, namely, electronic chemical potential μ, chemical hardness η, global electrophilicity ω, and global nucleophilicity N for the 2POX, aniline, morpholine and for both complexes, namely 2POX–Fe, and 2POX–Sr were calculated and reported in Table 8. From the obtained results, we can notice that in the absence of metal the electronic chemical potential of the secondary amine (morpholine), $\mu = -1.74$ eV, is higher than that of 2POX, $\mu = -3.85$ eV, indicating that at the TSs, the GEDT will take place from the morpholine compound towards the 2POX. In the case of primary amine (aniline), a similar chemical potential value was obtained which can explain the absence of products in this case. The coordination of 2POX with metals increases the chemical potential value that conducts to a GEDT from 2POX–metals to primary
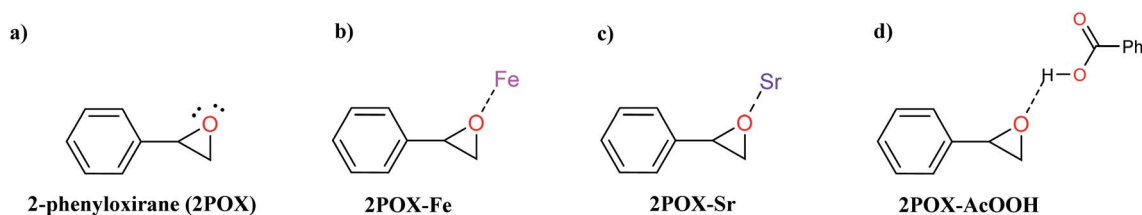
Scheme 5 Schematic representation of the possible coordinating modes between SrFe-GO catalyst and 2-phenyloxirane (2POX).
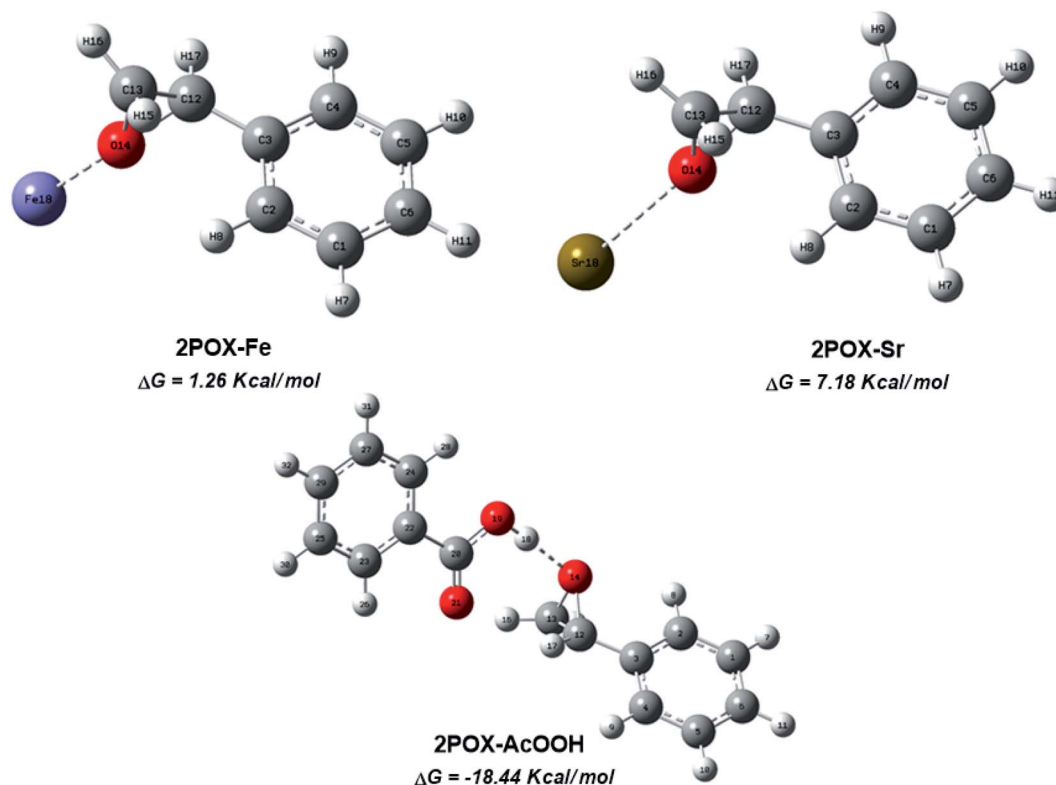
2POX-Fe
$\Delta G = 1.26\ Kcal/mol$

2POX-Sr
$\Delta G = 7.18\ Kcal/mol$

2POX-AcOOH
$\Delta G = -18.44\ Kcal/mol$

Fig. 9 Optimized structures of 2POX–SrFe-GO complexes.

Table 8 Global electronic proprieties and reactivity indexes, values were reported in eV

	HOMO	LUMO	μ	η	ω	N
2POX	−6.50	−0.21	−3.36	6.29	0.89	2.61
Aniline	−6.54	0.02	−3.26	6.56	0.81	2.57
Morpholine	−5.71	2.22	−1.74	7.94	0.19	3.40
2POX–Fe	−3.62	−1.74	−2.68	1.89	1.90	5.49
2POX–Sr	−3.37	−0.75	−2.06	2.62	0.81	5.74
2POX–AcOOH	−6.66	−1.08	−3.87	5.58	1.34	2.45

amine (aniline) and the inverse in the case of secondary amine (Table 8). The global electrophilicity and nucleophilicity indexes of reactants were calculated, see Table 8. The results indicate that the 2POX acts as a moderate electrophile ($\omega = 0.89$ eV) and moderate nucleophile ($N = 2.61$ eV). Similar results were obtained in the case of primary amine (aniline) while morpholine acts as a stronger nucleophile compared to aniline. The coordination of 2POX with metals conducts to a strong nucleophile ($N = 5.49$ eV) and a moderate electrophile ($\omega = 1.90$ eV), for 2POX–Fe, and a marginal electrophile ($\omega = 1.90$ eV) and a strong nucleophile ($N = 5.49$ eV) in the case of 2POX–Sr within the electrophilicity[97] and nucleophilicity scales.[98] These results confirm that along with this reaction the 2POX–Fe acts as an electrophile and the amines as a nucleophile with a large polar character.

Along a polar reaction, the bond-forming process takes place at a specific position of a molecule and can explain the regio- or chemoselectivity issues of the reaction. In this regard, the epoxide ring-opening reaction in which the different approach modes of a reagent towards the other can yield two competitive isomers. The analysis of the local electrophilicity ω_k at the electrophilic reagent and the local nucleophilicity N_k at the nucleophilic one derived from Parr functions allows us to explain the regioselectivity that is experimentally observed in the organic reactions with a large polar character.[99] Therefore, the values of the electrophilic and nucleophilic Parr functions, the local electrophilicity, and the local nucleophilicity at the 2POX, aniline, morpholine, 2POX–Fe, 2POX–Sr, and 2POX–AcOOH are calculated and summarized in Fig. 10.

The analysis of the local electrophilicity ω_k at 2POX indicates that the carbon atom C_1 is the more electrophilically activated center in this compound, $\omega_k (C_1) = 0.064$ eV and the analysis of the local nucleophilicity at amines indicates that the nitrogen atom is the most nucleophilic center, $N_k (N_1) = 1.112$ and 1.771 eV for aniline and morpholine, respectively. These results confirm the selective synthesis of compound **3** in absence of catalyst (see Table 3, entry 5). The coordination of 2POX with metals indicates that the presence of iron atoms conducts to the synthesis of compound **4** while the presence of strontium atoms leads to the selective synthesis of compound **3**. In the case of the coordination of 2POX with acid function, the findings show that the most electrophilic center is located in the carbon (C_1) atom. Consequently, the most favorable bond formation will correspond to the N_1 (amines) → C1 (2POX–AcOOH), leading to the formation of compound **3** (see Table 3, entries 1 and 4). All these
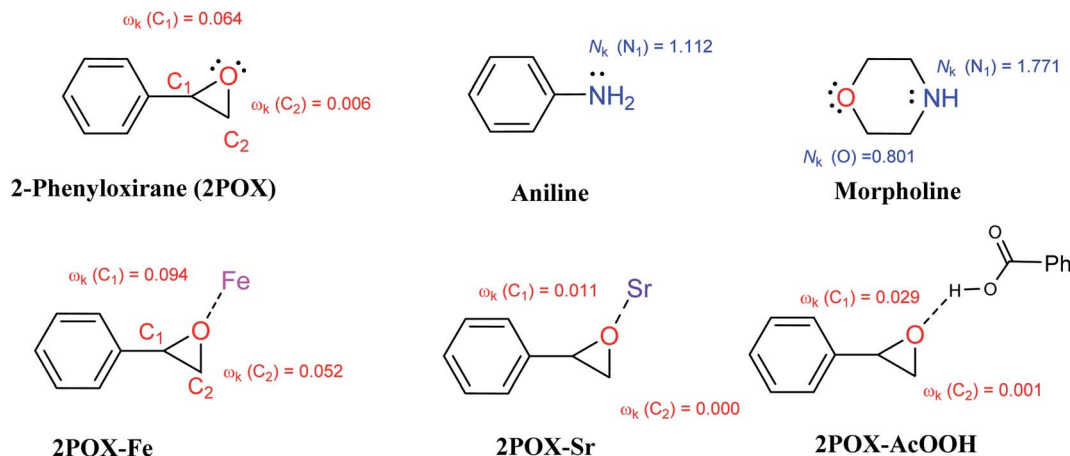
Fig. 10 Local electrophilicity ω_k (in red color) and local nucleophilicity N_k (in blue color) calculated using Parr function and all presented values are in eV.

results are in good agreement with the experimental observations and can explain the important role of iron, strontium atoms, and acid function in the improvement of the conversion and selectivity in the epoxide ring-opening reactions.

To get more light on the synergy effect between iron and strontium atoms for regioselective ring-opening of epoxides in the presence of amines, proposed models of the prepared catalyst was investigated using cluster metal atoms for the accepted mechanism to understand the selectivity obtained in the synthesis of

compounds **3** and **6** using SrFe-GO catalyst (Fig. 11). Firstly, the formation of a bond between amine groups and epoxide is performed through a transition state, TSA for aniline and TSB for morpholine. The results indicate that these TSs are endothermic in both phases, in the absence and presence of catalysis. In the absence of catalyst, the computed barrier for the formation of the first N_1–C_1 single bond *via* TSA using aniline is 33.74 kcal mol^{-1}, a value that is slightly higher than the barrier for TSB using morpholine (*ca.* 31.77 kcal mol^{-1}). The epoxide ring-opening
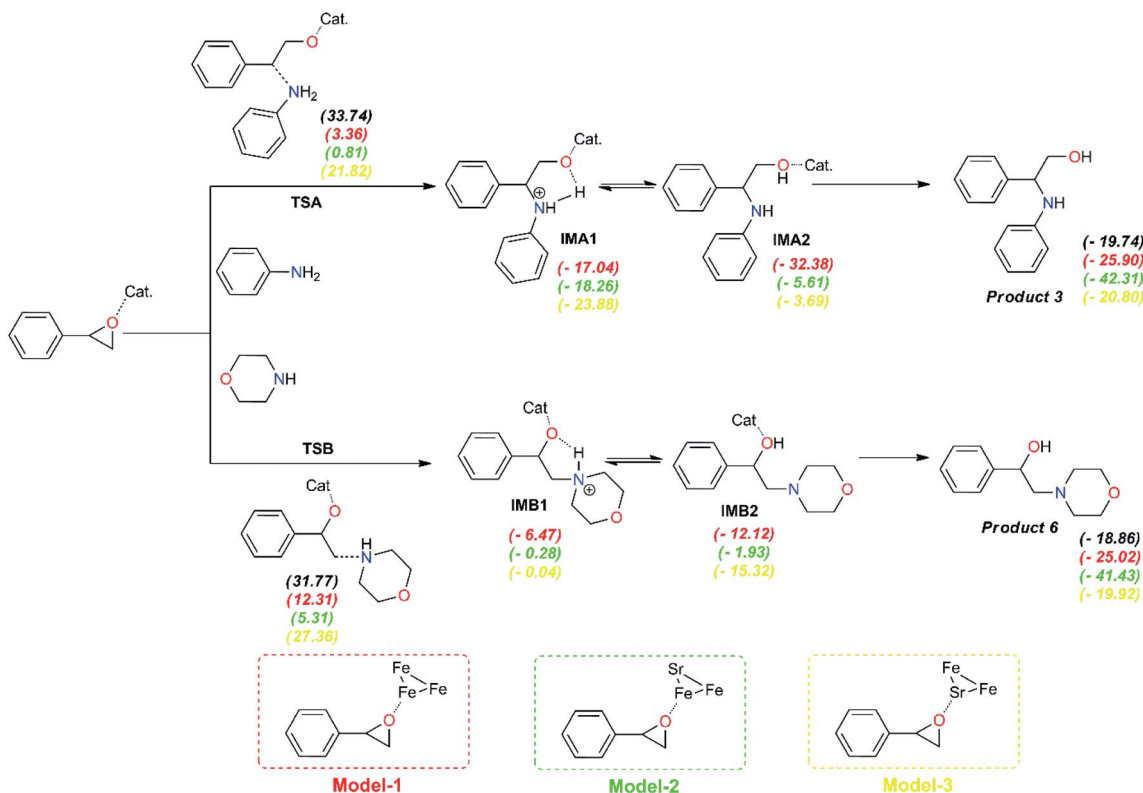

Fig. 11 DFT-computed energy profiles of the uncatalyzed epoxide ring-opening (values in black) and in presence of three models of SrFe-GO catalyst: model-1 (values in red), model-2 (values in green), and model-3 (values in yellow). All values are reported in kcal mol^{-1}.

using FeSr cluster (model-3) has a higher energetic barrier in the case of aniline, $\Delta E(\text{TSA}) = 21.82$ kcal mol^{-1}, and also in the case of morpholine, $\Delta E(\text{TSA}) = 27.36$ kcal mol^{-1}. In the case of the Fe3 cluster (model-1), the energetic barrier of transition states (TSs) is reduced by $\sim$14 kcal mol^{-1} for both amines. Interestingly, the presence of the SrFe cluster (model-2) can reduce this energetic barrier in the case of aniline, $\Delta E(\text{TSA}) = 0.81$ kcal mol^{-1}, and also in the case of morpholine, $\Delta E(\text{TSB}) = 5.31$ kcal mol^{-1}. All obtained intermediates using models of SrFe catalyst are exothermic. Subsequently, the formation of products **3** and **6** are exothermic in all cases. These results allow us to explain the synergy effect between iron and strontium atoms for regioselective ring-opening of epoxides in the presence of amines and the role of metal nature especially iron in the selectivity of the corresponding products.

4. Conclusion

In a summary, we have reported a successful synthesis of magnetically separable hybrid GO/SrFe$_{12}$O$_{19}$ nanocomposite. First, the SrFe$_{12}$O$_{19}$ NPs were synthesized by a chemical coprecipitation method, while the GO sheets were prepared by the chemical oxidation of graphite powder. For comparison purposes, reduced graphene oxide (rGO) and rGO/SrFe$_{12}$O$_{19}$ were prepared respectively by reducing GO sheets and the prepared hybrid material. The characterization of GO/SrFe$_{12}$O$_{19}$, rGO/SrFe$_{12}$O$_{19}$, and pure SrFe$_{12}$O$_{19}$ by XRD presents the same corresponding diffraction patterns of M-type hexagonal ferrites structure. FTIR spectra of prepared materials exhibit the characteristic bands of GO (rGO) and SrFe$_{12}$O$_{19}$ in the hybrid GO/SrFe$_{12}$O$_{19}$ (rGO/SrFe$_{12}$O$_{19}$). However, FESEM-EDX analyses reveal an excellent morphology and homogeneity in composition. Moreover, the prepared nanocomposites show good dispersed and distributed SrFe$_{12}$O$_{19}$ NPs on the surface of GO and rGO sheets. The prepared hybrid nanocomposite GO/SrFe$_{12}$O$_{19}$ exhibits an excellent catalytic activity with an easy magnetic reusability and good stability for the regioselective ring-opening reaction in neat water. The marked catalytic activity of the hybrid nanocomposite compared to pure SrFe$_{12}$O$_{19}$ is probably due to the synergistic effect created between GO and SF NPs. The ZP values indicated a higher stability of SF NPs in the hybrid compared to the pure ones, confirming that hybrid magnetic nanocomposite is an efficient heterogeneous catalyst compared to pure ferrite NPs. In addition, a mechanistic study through DFT calculation was used to explain the synergetic role between iron and strontium atoms in the total regioselectivity of SrFe-GO catalyst in epoxide ring-opening reaction, and the obtained results are in excellent agreement with the experimental observations.

Disclosure

The present research is a part of a PhD thesis work of the author Mouhsine Laayati.

Conflicts of interest

The authors declare that they have no conflicts of interest.

Acknowledgements

References

1 S. E. McNeil, *J. Leukoc. Biol.*, 2005, **78**, 585–594.

2 A. Owen, C. Dufès, D. Moscatelli, E. Mayes, J. F. Lovell, K. V. Katti, K. Sokolov, M. Mazza, O. Fontaine, S. Rannard and V. Stone, *Nanomedicine*, 2014, **9**, 1291–1294.

3 L. H. Reddy, J. L. Arias, J. Nicolas and P. Couvreur, *Chem. Rev.*, 2012, **112**, 5818–5878.

4 N. Dasgupta, S. Ranjan and C. Ramalingam, *Environ. Chem. Lett.*, 2017, **15**, 591–605.

5 Z. Abdin, M. A. Alim, R. Saidur, M. R. Islam, W. Rashmi, S. Mekhilef and A. Wadi, *Renew. Sustain. Energy Rev.*, 2013, **26**, 837–852.

6 W. Y. Kim, Y. C. Choi, S. K. Min, Y. Cho and K. S. Kim, *Chem. Soc. Rev.*, 2009, **38**, 2319–2333.

7 F. Soofivand, F. Mohandes and M. Salavati-Niasari, *Mater. Res. Bull.*, 2013, **48**, 2084–2094.

8 F. Motahari, M. R. Mozdianfard, F. Soofivand and M. Salavati-Niasari, *RSC Adv.*, 2014, **4**, 27654–27660.

9 A. R. Armstrong and P. G. Bruce, *Nature*, 1996, **381**, 499–500.

10 M. Yousefi, F. Gholamian, D. Ghanbari and M. Salavati-Niasari, *Polyhedron*, 2011, **30**, 1055–1060.

11 S. Ibraheem, G. Yasin, A. Kumar, M. A. Mushtaq, S. Ibrahim, R. Iqbal, M. Tabish, S. Ali and A. Saad, *Appl. Catal. B Environ.*, 2022, **304**, 120987.

12 M. Arif, G. Yasin, L. Luo, W. Ye, M. A. Mushtaq, X. Fang, X. Xiang, S. Ji and D. Yan, *Appl. Catal. B Environ.*, 2020, **265**, 118559.

13 O. Mohanta, Y. N. Singhbabu, S. K. Giri, D. Dadhich, N. N. Das and R. K. Sahu, *J. Alloys Compd.*, 2013, **564**, 78–83.

14 T. Ahmadi, G. Mohammadi Ziarani, S. M. Masoumian Hoseini, A. Badiei and M. M. Ranjbar, *J. Iran. Chem. Soc.*, 2021, **18**, 2047–2056.

15 E. Alimohammadi, S. Sheibani and A. Ataie, *Mater. Chem. Phys.*, 2022, **275**, 125312.

16 S. Chen, Y. Di, H. Li, M. Wang, B. Jia, R. Xu and X. Liu, *Appl. Surf. Sci.*, 2021, **559**, 149855.

17 R. C. Pullar, *Prog. Mater. Sci.*, 2012, **57**, 1191–1334.

18 E. Govea-Alcaide, J. Matilla-Arias, F. Guerrero, P. Mariño-Castellanos, K. Montero-Rey, F. Rosales-Saiz and I. F. Machado, *J. Magn. Magn. Mater.*, 2021, **533**, 167966.

19 X. Zhu, X. Wang, K. Liu, H. Yuan, R. Boudaghi and M. N. Akhtar, *J. Alloys Compd.*, 2021, **873**, 159818.

20 S. S. Nikitin, O. V. Merkulov, A. D. Bamburov and M. V. Patrakeev, *J. Alloys Compd.*, 2021, **873**, 159677.

21 J. L. Gong, B. Wang, G. M. Zeng, C. P. Yang, C. G. Niu, Q. Y. Niu, W. J. Zhou and Y. Liang, *J. Hazard. Mater.*, 2009, **164**, 1517–1522.

22 L. Chen, Z. Xu, H. Dai and S. Zhang, *J. Alloys Compd.*, 2010, **497**, 221–227.

23 M. D. Kaminski and L. Nuñez, *J. Magn. Magn. Mater.*, 1999, **194**, 31–36.

24 C. Chen, J. Hu, D. Shao, J. Li and X. Wang, *J. Hazard. Mater.*, 2009, **164**, 923–928.

25 S. Imine, F. Schoenstein, S. Mercone, M. Zaghrioui, N. Bettahar and N. Jouini, *J. Eur. Ceram. Soc.*, 2011, **31**, 2943–2955.

26 J. Ding, C. Zhou, Z. Wu, C. Chen, N. Feng, L. Wang, H. Wan and G. Guan, *Appl. Catal. Gen.*, 2021, **616**, 118080.

27 Y. Zhang, B. Chen, L. Zhang, J. Huang, F. Chen, Z. Yang, J. Yao and Z. Zhang, *Nanoscale*, 2011, **3**, 1446–1450.

28 J. Yan, T. Wei, W. Qiao, B. Shao, Q. Zhao, L. Zhang and Z. Fan, *Electrochim. Acta*, 2010, **55**, 6973–6978.

29 Y. Zhu, S. Murali, W. Cai, X. Li, J. W. Suk, J. R. Potts and R. S. Ruoff, *Adv. Mater.*, 2010, **22**, 3906–3924.

30 G. Eda and M. Chhowalla, *ACS Nano*, 2011, **5**, 4265–4268.

31 G. Yasin, M. Arif, T. Mehtab, M. Shakeel, M. A. Mushtaq, A. Kumar, T. A. Nguyen, Y. Slimani, M. T. Nazir and H. Song, *Inorg. Chem. Front.*, 2020, **7**, 402–410.

32 M. A. Mushtaq, M. Arif, X. Fang, G. Yasin, W. Ye, M. Basharat, B. Zhou, S. Yang, S. Ji and D. Yan, *J. Mater. Chem. A*, 2021, **9**, 2742–2753.

33 G. Yasin, S. Ibraheem, S. Ali, M. Arif, S. Ibrahim, R. Iqbal, A. Kumar, M. Tabish, M. A. Mushtaq, A. Saad, H. Xu and W. Zhao, *Mater. Today Chem.*, 2022, **23**, 100634.

34 S. Ebrahimpoor, V. Kiarostami, M. Khosravi, M. Davallo and A. Ghaedi, *Fibers Polym.*, 2021, **22**, 159–170.

35 A. Aziz, Y. H. Yau, G. L. Puma, C. Fischer, S. Ibrahim and S. Pichiah, *Chem. Eng. J.*, 2014, **235**, 264–274.

36 J. Luo, P. Shen, W. Yao, C. Jiang and J. Xu, *Nanoscale Res. Lett.*, 2016, **11**, 141.

37 C. Zhao, M. Shen, Z. Li, R. Sun, A. Xia and X. Liu, *J. Alloys Compd.*, 2016, **689**, 1037–1043.

38 M. T. Barros, M. A. J. Charmier, C. D. Maycock and T. Michaud, *Tetrahedron*, 2005, **61**, 7960–7966.

39 E. J. Corey and F. Y. Zhang, *Angew. Chem. Int. Ed.*, 1999, **38**, 1931–1934.

40 C. W. Johannes, M. S. Visser, G. S. Weatherhead and A. H. Hoveyda, *J. Am. Chem. Soc.*, 1998, **120**, 8340–8347.

41 S. Pulla, C. M. Felton, Y. Gartia, P. Ramidi and A. Ghosh, *ACS Sustain. Chem. Eng.*, 2013, **1**, 309–312.

42 D. J. Ager, I. Prakash and D. R. Schaad, *Chem. Rev.*, 1996, **96**, 835–875.

43 Y. He, H. Lu, X. Li, J. Wu, T. Pu, W. Du, H. Li, J. Ding, H. Wan and G. Guan, *Green Chem.*, 2021, **23**, 8571–8580.

44 Y. He, X. Li, W. Cai, H. Lu, J. Ding, H. Li, H. Wan and G. Guan, *ACS Sustain. Chem. Eng.*, 2021, **9**, 7074–7085.

45 M. Palmer, T. Walsgrove and M. Wills, *J. Org. Chem.*, 1997, **62**, 5226–5228.

46 E. Alza, A. Bastero, S. Jansat and M. A. Pericàs, *Tetrahedron: Asymmetry*, 2008, **19**, 374–378.

47 A. Patti and S. Pedotti, *Tetrahedron: Asymmetry*, 2003, **14**, 597–602.

48 Y. Fujiwara, T. Katagiri and K. Uneyama, *Tetrahedron Lett.*, 2003, **44**, 6161–6163.

49 Y. F. Kang, R. Wang, L. Liu, C. S. Da, W. J. Yan and Z. Q. Xu, *Tetrahedron Lett.*, 2005, **46**, 863–865.

50 W. Oppolzer and R. N. Radinov, *Tetrahedron Lett.*, 1988, **29**, 5645–5648.

51 N. Azizi and M. R. Saidi, *Tetrahedron*, 2007, **63**, 888–891.

52 J. Agarwal, A. Duley, R. Rani and R. Peddinti, *Synthesis*, 2009, **2009**, 2790–2796.

53 R. Outouch, M. Rauchdi, B. Boualy, L. El Firdoussi, A. Roucoux and M. A. Ali, *Acta Chim. Slov.*, 2014, **61**, 67–72.

54 A. T. Placzek, J. L. Donelson, R. Trivedi, R. A. Gibbs and S. K. De, *Tetrahedron Lett.*, 2005, **46**, 9029–9034.

55 G. Sabitha, G. S. Kumar Reddy, K. Bhaskar Reddy and J. S. Yadav, *Synthesis*, 2003, **15**, 2298–2300.

56 M. C. Singh and R. K. Peddinti, *Tetrahedron Lett.*, 2007, **48**, 7354–7357.

57 J. R. Rodríguez and A. Navarro, *Tetrahedron Lett.*, 2004, **45**, 7495–7498.

58 M. Laayati, A. Hasnaoui, N. Abdallah, S. Oubaassine, L. Fkhar, O. Mounkachi, S. El Houssame, M. Ait Ali and L. El Firdoussi, *J. Chem.*, 2020, **2020**, 1–10.

59 M. J. Frisch, G. W. Trucks, H. B. Schlegel, G. E. Scuseria, M. A. Robb, J. R. Cheeseman, G. Scalmani, V. Barone, B. Mennucci, G. A. Petersson, H. Nakatsuji, M. Caricato, X. Li, H. P. Hratchian, A. F. Izmaylov, J. Bloino, G. Zheng, J. L. Sonnenberg, M. Hada, M. Ehara, K. Toyota, R. Fukuda, J. Hasegawa, M. Ishida, T. Nakajima, Y. Honda, O. Kitao, H. Nakai, T. Vreven, J. A. Montgomery Jr, J. E. Peralta, F. Ogliaro, M. Bearpark, J. J. Heyd, E. Brothers, K. N. Kudin, V. N. Staroverov, R. Kobayashi, J. Normand, K. Raghavachari, A. Rendell, J. C. Burant, S. S. Iyengar, J. Tomasi, M. Cossi, N. Rega, J. M. Millam, M. Klene, J. E. Knox, J. B. Cross, V. Bakken, C. Adamo, J. Jaramillo, R. Gomperts, R. E. Stratmann, O. Yazyev, A. J. Austin, R. Cammi, C. Pomelli, J. W. Ochterski, R. L. Martin, K. Morokuma, V. G. Zakrzewski, G. A. Voth, P. Salvador, J. J. Dannenberg, S. Dapprich, A. D. Daniels, Ö. Farkas, J. B. Foresman, J. V. Ortiz, J. Cioslowski and D. J. Fox, *Gaussian 09*, Gaussian Inc, Wallingford CT, 2009.

60 A. D. Becke, *J. Chem. Phys.*, 1993, **98**, 5648–5652.

61 C. Lee, W. Yang and R. G. Parr, *Phys. Rev. B: Condens. Matter Mater. Phys.*, 1988, **37**, 785–789.

62 L. E. Roy, P. J. Hay and R. L. Martin, *J. Chem. Theory Comput.*, 2008, **4**, 1029–1031.

63 R. G. Parr, L. V. Szentpály and S. Liu, *J. Am. Chem. Soc.*, 1999, **121**, 1922–1924.

64 L. R. Domingo and P. Pérez, *Org. Biomol. Chem.*, 2011, **9**, 7168–7175.

65 L. R. Domingo, P. Pérez and J. A. Sáez, *RSC Adv.*, 2013, **3**, 1486–1494.

66 B. Delley, *J. Chem. Phys.*, 2000, **113**, 7756–7764.

67 J. P. Perdew, K. Burke and M. Ernzerhof, *Phys. Rev. Lett.*, 1996, **77**, 3865–3868.

68 M. Ernzerhof and G. E. Scuseria, *J. Chem. Phys.*, 1999, **110**, 5029–5036.

69 Y. Inada and H. Orita, *J. Comput. Chem.*, 2008, **29**, 225–232.

70 P. Sivakumar, L. Shani, Y. Yeshurun, A. Shaulov and A. Gedanken, *J. Mater. Sci. Mater. Electron.*, 2016, **27**, 5707–5714.

71 P. Scherrer, in *Kolloidchemie Ein Lehrbuch*, Springer Berlin Heidelberg, Berlin, Heidelberg, 1912, pp. 387–409.

72 X. Meng, Y. Zhu, S. Xu and T. Liu, *RSC Adv.*, 2016, **6**, 4946–4949.

73 T. Ben Ghzaiel, W. Dhaoui, A. Pasko and F. Mazaleyrat, *J. Alloys Compd.*, 2016, **671**, 245–253.

74 M. A. Almessiere, Y. Slimani, H. Güngüneş, A. Baykal, S. V. Trukhanov and A. V. Trukhanov, *Nanomaterials*, 2019, **9**, 1–18.

75 L. Zhang and Z. Li, *J. Alloys Compd.*, 2009, **469**, 422–426.

76 G. P. Nethala, R. Tadi, G. R. Gajula, K. N. Chidambara Kumar and V. Veeraiah, *Phys. B Condens. Matter*, 2018, **550**, 136–144.

77 Z. Lin, Y. Yao, Z. Li, Y. Liu, Z. Li and C. P. Wong, *J. Phys. Chem. C*, 2010, **114**, 14819–14825.

78 Y. Yao, Z. Yang, D. Zhang, W. Peng, H. Sun and S. Wang, *Ind. Eng. Chem. Res.*, 2012, **51**, 6044–6051.

79 X. Huang, Z. Yin, S. Wu, X. Qi, Q. He, Q. Zhang, Q. Yan, F. Boey and H. Zhang, *Small*, 2011, **7**, 1876–1902.

80 B. Mouhsine, A. Karim, C. Dumont and M. Sauthier, *Green Chem.*, 2020, **22**, 950–955.

81 G. W. Lu and P. Gao, in *Handbook of Non-Invasive Drug Delivery Systems*, Elsevier, 2010, pp. 59–94.

82 A. J. Shnoudeh, I. Hamad, R. W. Abdo, L. Qadumii, A. Y. Jaber, H. S. Surchi and S. Z. Alkelany, in *Biomaterials and Bionanotechnology*, Elsevier, 2019, pp. 527–612.

83 R. S. Vithalani, C. K. Modi, V. Sharma, P. K. Jha and H. Srivastava, *J. Mol. Struct.*, 2022, **1249**, 131620.

84 B. P. Shivani and A. K. Chakraborti, *J. Org. Chem.*, 2007, **72**, 3713–3722.

85 M. Hosseini-Sarvari, *Can. J. Chem.*, 2008, **86**, 65–71.

86 N. Azizi, P. Kamrani and M. Saadat, *Appl. Organomet. Chem.*, 2016, **30**, 431–434.

87 S. Liu, J. Xie, W. Li, W. Kong, L. Wang and Q. Zhou, *Org. Lett.*, 2009, **11**, 4994–4997.

88 G. Kumar, R. Kumar, G. Ogruc-ildiz, R. Fausto and A. Husain, *J. Mol. Struct.*, 2019, **1177**, 33–46.

89 A. Iqbal, T. K. Hou, U. S. Shaari, F. Adam and N. H. H. A. Bakar, *Mater. Today Proc.*, 2018, **5**, 21584–21593.

90 B. Tang, W.-C. Song, S.-Y. Li, E.-C. Yang and X.-J. Zhao, *New J. Chem.*, 2018, **42**, 13503–13511.

91 A. V Nakhate and G. D. Yadav, *ChemistrySelect*, 2018, **3**, 4547–4556.

92 A. Sheoran, M. Dhiman, S. Bhukal, R. Malik, J. Agarwal, B. Chudasama and S. Singhal, *Mater. Chem. Phys.*, 2019, **222**, 207–216.

93 S. Verma, H. P. Mungse, N. Kumar, S. Choudhary, S. L. Jain, B. Sain and O. P. Khatri, *Chem. Commun.*, 2011, **47**, 12673–12675.

94 A. A. Mekkaoui, H. Ben El Ayouchia, H. Anane, R. Chahboun, L. El Firdoussi and S. El Houssame, *J. Mol. Struct.*, 2021, **1235**, 130221.

95 P. Geerlings, F. De Proft and W. Langenaeker, *Chem. Rev.*, 2003, **103**, 1793–1873.

96 L. Domingo, M. Ríos-Gutiérrez and P. Pérez, *Molecules*, 2016, **21**, 748.

97 L. R. Domingo, M. J. Aurell, P. Pérez and R. Contreras, *Tetrahedron*, 2002, **58**, 4417–4423.

98 P. Jaramillo, L. R. Domingo, E. Chamorro and P. Pérez, *J. Mol. Struct.*, 2008, **865**, 68–72.

99 L. R. Domingo, *RSC Adv.*, 2014, **4**, 32415–32428.